Biophysical Chemistry 284 (2022) 106793

Contents lists available at ScienceDirect

Biophysical Chemistry

journal homepage: www.elsevier.com/locate/biophyschem

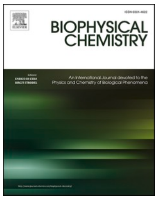

Biocementation of soils of different surface chemistries via enzyme induced carbonate precipitation (EICP): An integrated laboratory and molecular dynamics study

Hamid Ghasemi [a], S. Milad Hatam-Lee [b], Hamed Khodadadi Tirkolaei [c], Hessam Yazdani [a,*]

[a] Department of Civil and Environmental Engineering, Howard University, Washington, DC 20059, USA
[b] Department of Mechanical and Aerospace Engineering, The State University of New York at Buffalo, Buffalo, NY, USA
[c] School of Sustainable Engineering and the Built Environment, Arizona State University, Tempe, AZ 85287, USA

ARTICLE INFO

Keywords:
Biocementation
MICP
EICP
Ground improvement
Atomistic simulation
Ottawa sand

ABSTRACT

Biocementation is a ground improvement technique that involves precipitating a mineral (commonly calcium carbonate, $CaCO_3$) in the soil pore space to bind soil particles, in turn increasing the strength and reducing the permeability of the soil. Ureolysis (i.e. hydrolysis of urea) is the most researched calcium carbonate precipitation mechanism, which can be induced through either a microbial (MICP) or enzymatic (EICP) process. While laboratory tests and field trials have provided strong evidence of the efficacy of biocementation in strengthening granular materials, the role of the precipitate–grain interface and the surface chemistry of soil grains in biocementation are largely unknown. This study aims to address this gap. To this end, two geotechnically similar sand samples differing considerably in the amount of iron oxide and iron sulfate on grain surface are biocemented via EICP and tested for unconfined compressive strength (UCS). The biocemented sample containing a high concentration of iron oxide and iron sulfate exhibits almost 50% lower UCS than the other sample. To investigate whether surface chemistry can explain this considerable difference, interactions of $CaCO_3$ with quartz (SiO_2), hematite (Fe_2O_3), and marcasite (FeS_2) as polymorphs of silicon dioxide, iron oxide, and iron sulfide, respectively, are simulated using molecular dynamics. The influence of water content at the precipitate–grain interface is also considered. Simulation results indicate that in dry conditions, $CaCO_3$ has almost two times stronger affinity for SiO_2 than Fe_2O_3 and FeS_2, suggesting that biocementation is most effective for clean sands. It is also shown that water reduces the precipitate–grain adhesion.

1. Introduction

Biocementation is a potentially more sustainable alternative to ground improvement techniques that use additives with high embodied energy such as cement or environmentally harmful chemical stabilizers to treat problematic soils. It involves precipitating a mineral in the pores as a cementitious agent to bind soil particles, in turn increasing the strength, stiffness, dilatancy, and cyclic resistance of the soil and reducing its permeability. Laboratory studies and pilot field trials have demonstrated the efficacy of this technique in improving the bearing capacity of foundations [1], mitigating fluid and gas leakage through plugging wellbores [2,3], controlling fugitive dust [4], slope stabilization [5], water erosion control [6], land reclamation [7], liquefaction mitigation [8,9], and creating biocemented soil columns for ground improvement [10].

Precipitation of calcium carbonate ($CaCO_3$) via urea (CH_4N_2O) hydrolysis (a.k.a. ureolysis) is the most researched biocementation process [11]. This process involves microbial and enzymatic approaches where urease enzyme-producing bacteria and free urease enzymes extracted from microbes or plants are applied to catalyze ureolysis reactions to generate carbonate ($CO_3{}^{2-}$) and alkalinity, resulting in the precipitation of $CaCO_3$ in the presence of calcium ions, as shown in Eqs. 1 and 2:

$$CH_4N_2O + 2H_2O \xrightarrow{urease} 2NH_4^+ + CO_3^{2-} \tag{1}$$

$$Ca^{2+} + CO_3^{2-} \rightarrow CaCO_3 \tag{2}$$

The microbial process is referred to as microbially induced carbonate precipitation (MICP) [12,13]. The enzymatic approach is known as

---

* Corresponding author.
E-mail address: hessam.yazdani@howard.edu (H. Yazdani).

https://doi.org/10.1016/j.bpc.2022.106793
Received 13 December 2021; Received in revised form 25 February 2022; Accepted 2 March 2022

enzyme-induced carbonate precipitation (EICP) and circumvents the microbial processes (i.e. cultivation and fixation of bacteria) in MICP by using free urease enzymes [14–16].

Soil improvement using MICP and EICP typically involves incrementally enhancing strength by increasing the quantity of precipitation in the pores [17]. This approach, however, increases the cost and time of the treatment process because it entails applying multiple cycles of treatment and a higher concentration of ingredients. Therefore, efforts should be made to improve precipitation quality so that a target improvement level can be achieved at a lower quantity of precipitation. In this regard, understanding the underlying mechanisms that promote precipitation at interparticle contacts and lead to the formation of stronger calcium carbonate minerals with enhanced adhesion affinity for the surface of soil particles is imperative. Despite their merits and routine use in biocementation research, conventional laboratory tests cannot reveal and explain these mechanisms and how they are affected by the physics and chemistry of soil particles at the molecular level.

Molecular dynamics (MD) is a powerful technique in computational statistical mechanics that is used to study the temporal evolution (i.e. fluctuations and conformational changes) of atomistic and molecular systems [18]. MD simulations can handle a broad range of complexity at the nano- and microscales and provide insight into phenomena that would otherwise remain unobserved or poorly understood if only conventional laboratory characterization techniques were used. The demanding computational cost of MD simulations, however, bounds their applicability to length and time scales in the order of nanometers and nanoseconds. MD has extensively been used to study physical, chemical, and biological systems. Examples of the application of MD in the geo-biophysical chemistry context include studying the contact angle of soil minerals [19], phase composition behavior of nano-size pores in frozen soils [20], oil recovery [21], soil sorptive potential [22], nucleation of heavy metals on clay particles [23,24], flocculation and aggregation of clay particles [25], and efficacy of bioderived molecules in reducing the diffusion of free radicals into bituminous composites [26]. To the best of our knowledge, however, MD has not been used to study the biocementation of soils.

In the present work, we used a combination of laboratory experiments and MD simulations to study the influence of grain surface chemistry and interfacial water content on the strength of sands biocemented via EICP. We treated two geotechnically similar sand samples of considerably different surface chemistries using EICP, as described in Section 2.1. The samples exhibited substantially different unconfined compressive strengths (Section 3.1). Described in Sections 2.2 and 3.2 are MD simulations that we carried out to probe the role of grain surface chemistry and interfacial water content in causing this difference.

2. Materials and methods

Details of the preparation and testing of EICP-treated sand samples and the MD simulations are provided in this section.

2.1. Laboratory experiments

Two different batches of the Ottawa 20/30 sand both conforming to ASTM C778 and found to be similar in geotechnical properties but distinct in chemical characteristics (Table 1) were biocemented using the EICP technique—Ottawa sand is naturally round and smooth grains of nearly pure quartz that is mined from deposits near Ottawa, Illinois, and Le Sueur, Minnesota—The two batches were purchased about eight years apart and are herein designated as Ottawa 1 (Fig. 1a) for the older batch and Ottawa 2 for the more recent one (Fig. 1b).

The EICP treatment solution used in this study comprised 1.0 M urea, 0.67 M calcium chloride dihydrate, and 50 mL/L jack bean crude extract (*Canavalia gladiata*) obtained from the process described in Ref. [28]. Columns of Ottawa 1 and Ottawa 2 sands, 102 mm (4 in) in height and 51 mm (2 in) in diameter, were prepared in acrylic columns. The bottom of the columns was closed with an adhesive cap to minimize leakage of the solution. The EICP solution was percolated from the top of the column until the sample was almost saturated (i.e. the amount of solution added was slightly more than the initial pore volume, ~80 mL, to ensure that the soil was soaked during the treatment). The treated columns were cured for a period of 36 h. At the end of the curing period, the pore solution was drained. This procedure was repeated two more times to complete a three-cycle treatment for each sample. Note that the amount of solution added in the second and third cycles was lower than in the first cycle due to pore-clogging. At the end of the treatment, the cemented sand columns were removed from the acrylic columns and placed in a water bath to remove soluble salt precipitates (Fig. 1c). After rinsing, the top and bottom surfaces of the treated sand columns were flattened using sandpaper and placed in a compression instrument to measure unconfined compressive strength (UCS)—the UCS test provides a quick measure of compressive strength for rocks and soils that possess sufficient cohesion to permit testing in the unconfined state—The final height-to-diameter ratio after flattening the surfaces was 1.5 (77/51 mm/mm). The columns were loaded to failure at a constant axial compression strain rate of 1.27 mm/min following ASTM D2166. The stress-strain plot was established, and the peak stress was considered as the strength of the specimen.

Table 1
Geotechnical and chemical characteristics of Ottawa 1 and Ottawa 2 [27].

	Property	Ottawa 1	Ottawa 2
Geotechnical Properties	Mean grain size (D_{50}) (mm)	0.73	0.73
	Coefficient of uniformity (C_u)	1.21	1.22
	Coefficient of curvature (C_c)	0.97	0.97
	Percentage passing 75-μm (No. 200) sieve	<0.1	<0.1
	Specific gravity (G_s)	2.66	2.66
	Maximum void ratio (e_{max})	0.69	0.78
	Minimum void ratio (e_{min})	0.46	0.50
Chemical Properties	pH of sand–DI* water suspension	9.1	4.5
	pH of sand–0.01 M $CaCl_2$ suspension	8.0	4.4
	EC of sand–DI water suspension (mS/m)	5	11
	[Mg^{2+}] in soil–DI water suspension (mM)	0.03	0.09
	[Ca^{2+}] in soil–DI water suspension (mM)	0.12	0.26
	[Cl^-] in soil–DI water suspension (mM)	0.16	0.15
	[$SO_4{}^{2-}$] in soil–DI water suspension (mM)	0.05	0.43
	Mass fraction of iron (g kg^{-1})	0.11	2.80
	Mass fraction of aluminum (g kg^{-1})	0.02	0.07

* deionized.

2.2. MD simulations

MD simulations were carried out to gain insight into the adsorption of calcium carbonate precipitates in both dry and hydrated conditions onto the grain surface of Ottawa 1 and Ottawa 2. Binding energy and work of adhesion (and the contribution of van der Waals [vdW] and electrostatic interactions to them) and density profiles of matter surrounding the grain surfaces were used to quantify, describe, and compare the absorptions and interactions involved.

Binding/interaction energy is derived by taking the difference in energy between the adsorbed/bound state and the isolated-components state. For a two-component system consisting of components m and n, the binding energy between m and n can be calculated as:

$$\Delta E_{\mathrm{mn}} = E_{\mathrm{mn}} - (E_{\mathrm{m}} + E_{\mathrm{n}}) \tag{3}$$

where E_{mn} is the total energy of the system in the adsorbed/bound state,

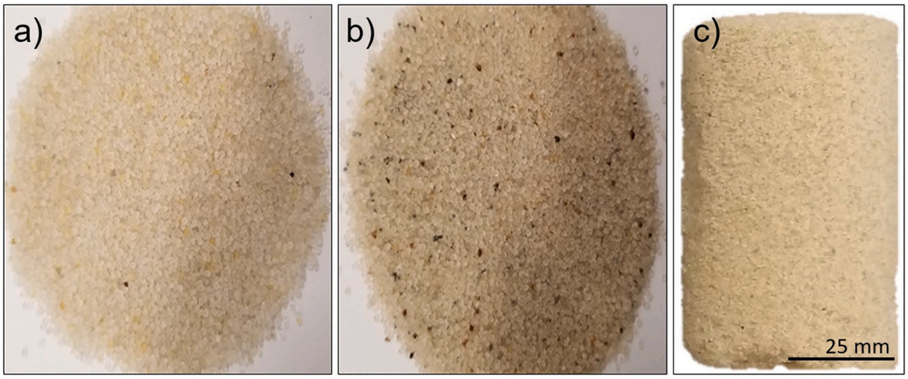

Fig. 1. Photos of a) Ottawa 1, b) Ottawa 2 (the darker texture is due to presence of iron oxide, Fe_2O_3, and iron sulfide, FeS_2, on grain surfaces), and c) Ottawa 1 after three EICP treatment cycles.

and E_m and E_n are the potential energies of components m and n in isolation and at thermodynamic equilibrium. ΔE_{mn} represents nonbonded interactions and consists of electrostatic (ΔE_{es}) and vdW (ΔE_{vdW}) interactions (depending on the system, it may include other contributions such as polar solvation energy and non-polar solvation energy [29]). A negative value for the binding energy of a bound system indicates adsorption (favorable gain in energy in the adsorbed state compared with the isolated state). Therefore, more negative values for binding energy mean that more energy must be supplied to the system to overcome the attractive force between the components [30,31].

Thermodynamic work of adhesion is defined as the energy required to separate a unit area of two components forming an interface and can be expressed as:

$$W_{mn} = \Delta E_{mn}/A \tag{4}$$

where A is the interfacial area between the components.

In the MD simulations, the calcium carbonate precipitates were considered to be composed of calcite crystals since the organic matter of the crude urease extract are unlikely to inhibit calcite precipitation in the soil [28], and no other agents (such as Mg^{2+}) favoring the formation of other polymorphs of calcium carbonate (i.e. aragonite and vaterite) were included in the treatment solution. There is also no report of the presence of non-calcite calcium carbonate polymorphs in the precipitates [32,33]. Note that $CaCO_3$, calcium carbonate, and calcite are hereafter interchangeably used. In addition to quartz (SiO_2) representing clean sands and silts, two mineral substrates of hematite (Fe_2O_3) and marcasite (FeS_2) were also included in the MD simulations. Precipitated from groundwater, these iron oxide and iron sulfide minerals exist in the St. Peter sandstone in the vicinity of Ottawa, Illinois, and Le Sueur, Minnesota, where Ottawa 20/30 is mined [34–37]. Ottawa 2 has been shown to contain a higher amount of iron and sulfate and is darker in color in comparison with Ottawa 1 [27], suggesting that the surface of Ottawa 2 grains is more heavily coated with iron oxide and iron sulfide.

The precipitates were modeled as dry and hydrated calcite. The dry models comprised a slab of calcite atop a substrate. The calcite slab consisted of 91 calcite unit cells each containing 12 calcite molecules. The substrates included quartz, hematite, and marcasite polymorphs of silicon dioxide, iron oxide, and iron sulfide, respectively. The unit cell information of calcite and the substrates was sourced from the American Mineralogist Crystal Structure Database [38], as summarized in Table 2.

Table 2
Unit cell dimensions of solid components of simulated models [38].

Material	a (Å)	b (Å)	c (Å)	α (°)	β (°)	γ (°)	Interacting surface orientation
Calcite	4.99	4.99	17.06	90	90	120	(104)
Fe_2O_3	5.04	5.04	13.77	90	90	120	(100)
FeS_2	3.37	4.44	5.39	90	90	90	(100)
SiO_2	4.92	4.92	5.40	90	90	120	(100)

The hydrated models were created by replacing the middle one, three, or five rows of calcite cells with H_2O molecules at a density of 1 g/cm^3, giving water contents (w_w) of 11%, 66%, and 200%—water content was defined as the mass of water per mass of dry calcite (i.e $w_w = m_{H2O}/m_{CaCO3}$). Fig. 2 shows the initial configuration of a 66% hydrated model

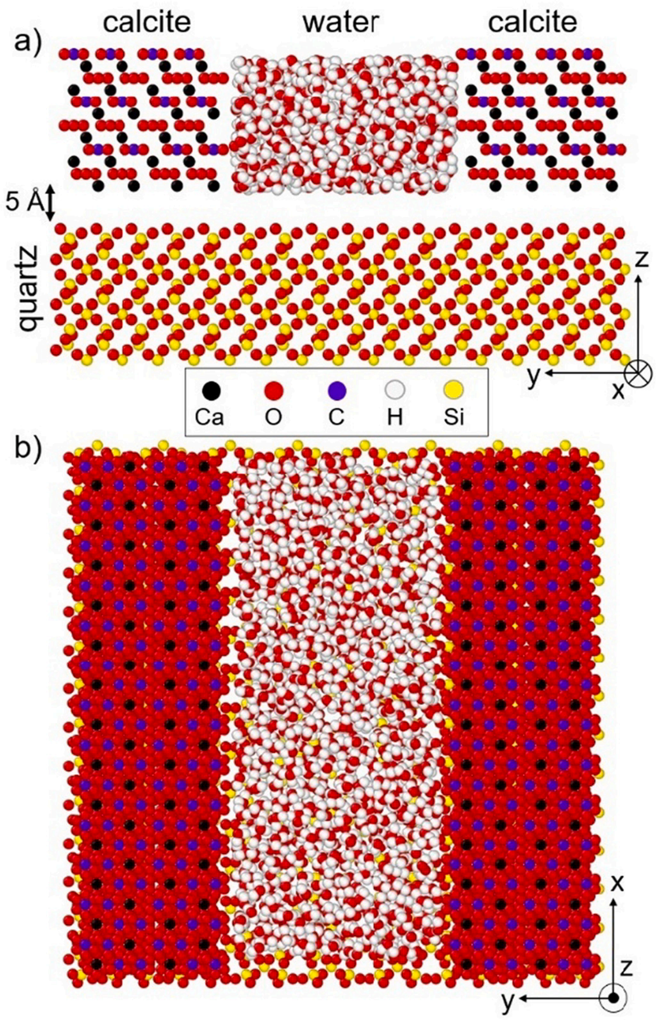

Fig. 2. a) side and b) top views of quartz–water-calcite model at $w_w = 66\%$. The 5-Å gap between the quartz slab and the calcite/water mixture was selected to be smaller than the cutoff distance.

over SiO_2 (quartz).

Assumptions adopted in the MD simulations included i) the crude urease extract would not interfere with the adhesion of the precipitates to the sand grain surface and ii) calcite crystals had already formed in the solution (i.e. no nucleation occurred on the grain surface).

Simulations were carried out with LAMMPS [39] and visualized with OVITO [40]. For each case, three simulations were performed with different seed numbers to account for randomness, and mean values and error bars are reported. Periodic boundary conditions in all directions and a time step of 1 fs were used in all simulations. The potentials used to describe interactions among the constituents are provided in Table 4. Nonbonded electrically neutral interactions were described by the Lennard–Jones (LJ) potential and the Lorentz-Berthelot rules, and long-range electrostatic interactions were solved by the PPPM method [41] with an accuracy of 10^{-4} on the forces (Table 3). Nonbonded interactions were truncated at a cutoff distance of 12 Å, the largest 2.5σ of all the atoms involved.

The dimensions of the components of the simulated models are summarized in Table 4. The thickness of the substrates (z dimension) was chosen to be greater than the cutoff distance of 12 Å to ensure that the bottom layer of atoms in the substrate would not interact with the precipitate, simulating a semi-infinite space.

The precipitate–substrate system was brought to relaxation by first placing the precipitate at an initial distance of 5 Å (< cutoff distance of 12 Å) above the substrate and then allowing it to interact with the substrate under the NPT ensemble until the energy of the system plateaued, indicating equilibrium. The energy and force convergence thresholds were set at 10^{-4} eV and 10^{-6} eV/Å, respectively. All simulations were carried out at 300 K using the Nosé–Hoover thermostat and barostat [47,48].

3. Results and discussion

3.1. Laboratory experiments (UCS tests)

Results of the UCS tests of EICP-treated Ottawa 1 and Ottawa 2 samples are shown in Fig. 3. The jagged shape of the plots, especially past the first peaks, points to spontaneous debonding along the shear band. The UCS of the treated Ottawa 1 sample peaked at 67.9 kPa at 0.8% axial strain and then fluctuated in a descending trend to reach 4.0 kPa at 4.0% axial strain. The UCS of the treated Ottawa 2 sample, in contrast, showed its first peak of 34.3 kPa at 1.1% strain and sustained it for 1.0% more strain before sharply falling to zero at 2.9% strain. The area under the stress–strain plots represents toughness (the total strain energy absorbed by the material before failure) and was calculated to be 75.4 and 48.6 J.m^{-3} for Ottawa 1 and Ottawa 2, respectively. Put another way, elastoplastic deformations in the treated Ottawa 1 sample resulted in the dissipation of 1.55 more energy before failure than that in the treated Ottawa 2 sample. This considerable difference in the behavior of these two geotechnically similar samples can be attributed to the significantly less amount of iron oxide and iron sulfide on the surface of the particles of Ottawa 1 compared with that of Ottawa 2. MD simulations shone light on this hypothesis, as described below.

Table 3
LJ and Coulomb values used for nonbonded interaction calculations.

Species	ε (eV)	σ (Å)	q (e)	Ref.
Ca [$CaCO_3$]	2.072805E-02	2.3700	+1.668E+00	[42]
C [$CaCO_3$]	3.824715E-03	3.8200	+9.990E-01	
O [$CaCO_3$]	6.031950E-03	3.0900	−8.890E-01	
C-O [$CaCO_3$]	2.718930E-01	1.1970	na	
O [H_2O]	4.423140E-03	3.1880	−8.300E-01	[43]
H [H_2O]	0.000000E+00	0.0000	+4.150E-01	
Fe [Fe_2O_3]	1.214200E-02	2.0900	+6.450E-01	[44]
O [Fe_2O_3]	1.084100E-02	2.4100	−4.300E-01	
Fe [FeS_2]	2.878080E-05	4.1564	+2.000E+00	[45]
S [FeS_2]	2.233252E-03	3.9064	−1.000E+00	
Si [SiO_2]	1.734500E-03	3.2000	+1.700E+00	[46]
O [SiO_2]	2.536852E-02	2.7000	−8.500E-01	

Table 4
Size of components of simulated models and respective force fields.

Component	x (Å) × y (Å) × z (Å)	Potential
$CaCO_3$	65.97 × 66.00 × 15.64	combination of Buckingham and harmonic bonding, bending, and torsion
FeS_2	70.02 × 71.04 × 16.17	Buckingham [49]
Fe_2O_3	70.53 × 69.80 × 13.77	Buckingham [49]
SiO_2	68.82 × 68.12 × 16.22	Tersoff [50]
H_2O	varied by weight fraction	TIP3P model [51]

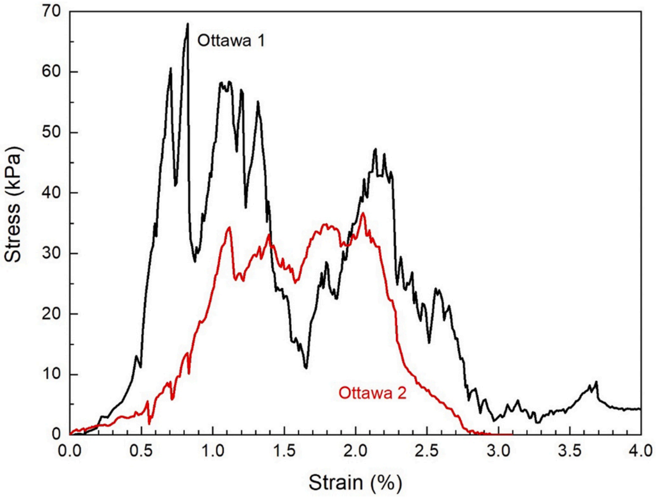

Fig. 3. Unconfined compressive stress-strain curve of EICP-treated Ottawa 1 sand (black) and EICP-treated Ottawa 2 sand (red). Strain rate = 1.27 mm/min. (For interpretation of the references to color in this figure legend, the reader is referred to the web version of this article.)

3.2. MD simulations

As an example, the history of binding energy between dry/hydrated calcite and the SiO_2 substrate as the configuration evolved from its initial state to the equilibrium (i.e. stable/relaxed) state is shown in Fig. 4. It can be seen that time to equilibrium decreased with increasing water content. This observation points to the hydrophilicity of quartz [52] and suggests that it has more affinity for water than calcite.

The influence of substrate and water content on the work of adhesion (*W*) between the precipitate and the substrates is shown in Fig. 5. Comparison of *W* values associated with dry conditions indicates that calcite had the strongest affinity for SiO_2, suggesting that stronger interfacial bonds are formed between calcite precipitates and the silica surface of the sands in the dry state (5.4 J/m^2 for SiO_2 vs. 2.7 J/m^2 and 3.0 J/m^2 for Fe_2O_3 and FeS_2, respectively). The ratio between the *W* of SiO_2 and the average *W* of Fe_2O_3 and FeS_2 (i.e. 2.9 J/m^2) is 1.89, which is, from the engineering perspective, in close agreement with the ratio of 1.55 calculated earlier for the toughness of the treated samples. Although surface chemistry and interfacial water content are expected to exhibit a heterogeneous distribution within soils, this good agreement between the *W* and toughness ratios provides evidence that toughness can capture and represent the changes in local binding energies within the samples as they undergo deformation. It can also be seen in Fig. 5 that while electrostatic and vdW interactions had comparable

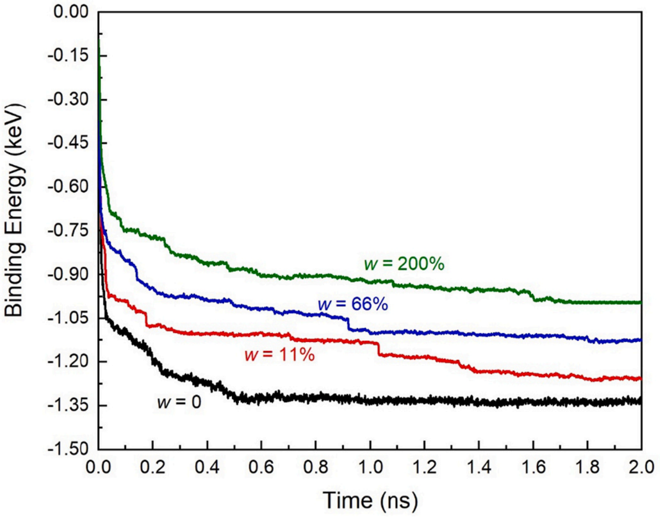

Fig. 4. History of binding energy between $CaCO_3$ and the SiO_2 substrate at different water contents. The energy level-off indicates equilibrium. More negative energy values indicate stronger binding.

contributions to W in dry FeS_2 and SiO_2 cases, that in the dry Fe_2O_3 case was overwhelmingly dominated by vdW interactions. This difference can be attributed to considerably higher charge densities in FeS_2 and SiO_2 than in Fe_2O_3 (Table 3).

Results shown in Fig. 5 indicate that hydration influenced the work of adhesion, W, differently, depending on the substrate. In the case of Fe_2O_3, W almost linearly decreased by 15% from the mean value of 2.7 J/m^2 in dry conditions to 2.3 J/m^2 at $w = 200\%$. W between FeS_2 and the precipitate remained practically insensitive to hydration. The $CaCO_3$–SiO_2 work of adhesion exhibited the highest susceptibility to the presence of water. It reduced by 20% from 5.4 J/m^2 to 4.3 J/m^2 upon the addition of 200% water to the interface and continued to sharply decrease at higher water contents. vdW interactions appeared to primarily be responsible for these reductions.

MD simulations also provided insight into the adsorption of aqueous species (O_{water} and H_{water}) and Ca onto the substrates. Fig. 6 shows the one-dimensional density profiles of these species as a function of distance from the substrates in dry and wet ($w_w = 66\%$) conditions. The height of the density profiles represents the percentage of each atom type in the vicinity of the substrates calculated by normalizing the number of atoms of a given type and host molecule in a region with respect to their total number in the entire model. Note that distance was calculated from the substrate atom having the highest z coordinate. Therefore, negative values of distance indicate penetration of the precipitate/water atoms, especially smaller atoms of H and O, into the substrate (see Fig. 7 for SiO_2).

Comparison of Fig. 6a (Ca in dry conditions) with Fig. 6b (Ca in hydrated conditions) indicates that the Ca atoms were partially displaced by the water molecules, explaining the overall reductions observed earlier in W as a result of hydration (Fig. 5) and suggesting a higher affinity of the substrates for water than for calcite. Density profiles of H_{water} and O_{water} in the vicinity of SiO_2 and FeS_2 are similar (Fig. 6c,d). In the vicinity of for Fe_2O_3 surface, however, a significant tail is observed for H_{water} toward the surface, suggesting preferential orientation of the water molecules on the surface and the formation of hydrogen bonds between water molecules and the surface. This reconfiguration of water molecules can be attributed to the hydrophilic character of Fe_2O_3 [53,54].

The relaxed configuration of precipitates ($w_w = 66\%$) on the substrates shown in Fig. 8 provides an account of the observations made from the density profiles. It can be seen that some water molecules diffused into the precipitate–substrate interface and partially displaced the calcite molecules (Supplementary Videos 1–12). It can also be observed that the water confined in the calcite slit rose along the slit walls to form a concave meniscus, indicating the hydrophilicity of calcite (i.e. calcite–water adhesion > water–water cohesion), as shown

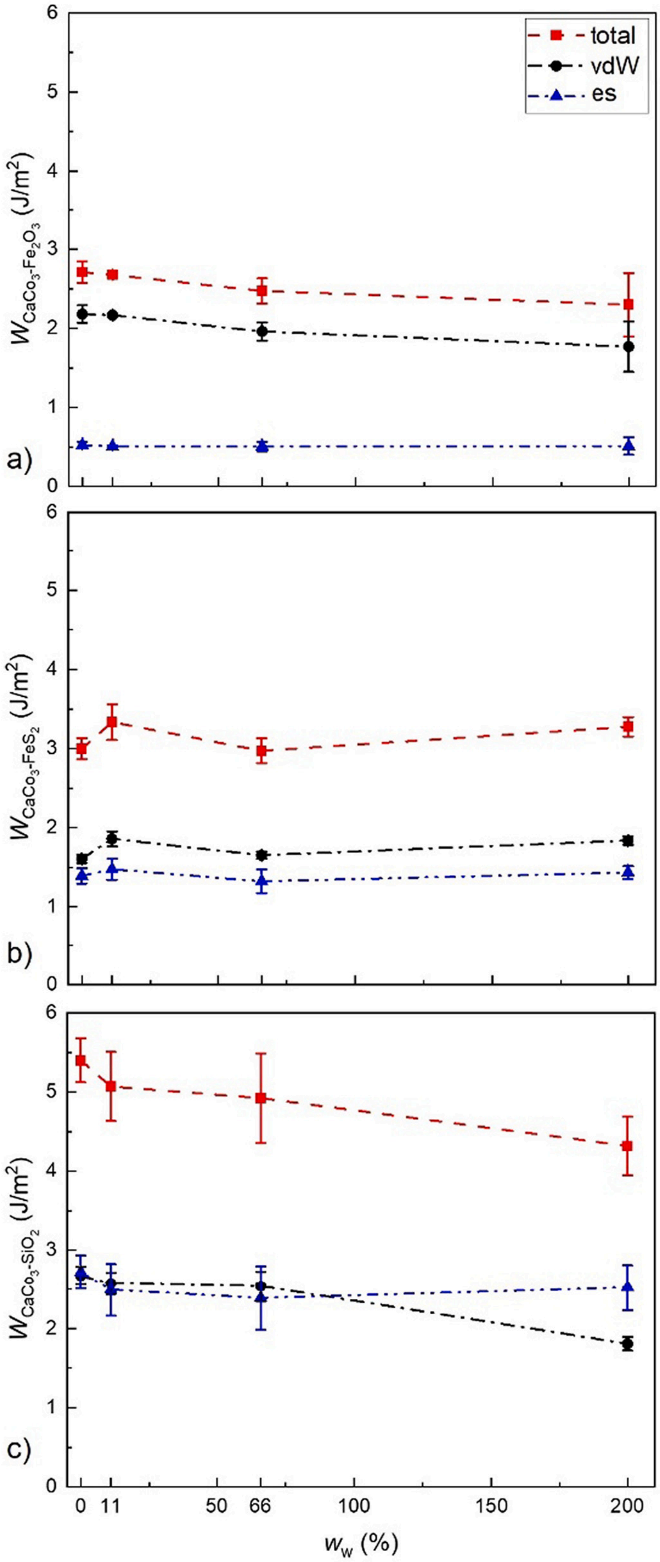

Fig. 5. Work of adhesion between calcite and a) Fe_2O_3, b) FeS_2, and c) SiO_2 substrates at different water contents. Contributions of vdW and electrostatic (es) interactions to the total energy are shown.

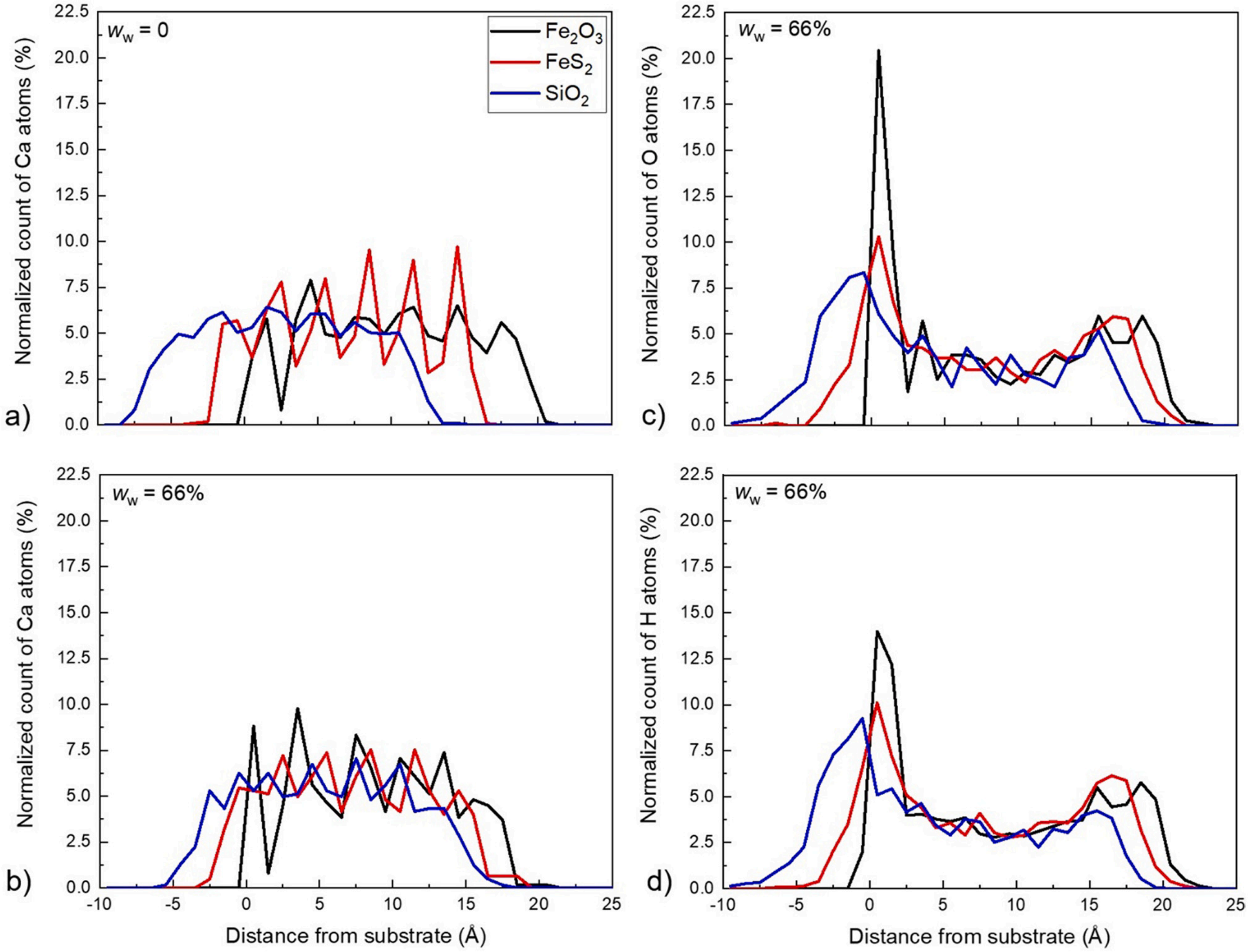

Fig. 6. Density profiles of a) Ca (dry), b) Ca (w_w = 66%), c) O_{H2O} (w_w = 66%), and d) H_{H2O} (w_w = 66%) atoms as a function of distance from the top atom of substrates. Negative distance values indicate penetration of the precipitate/water atoms into the substrate.

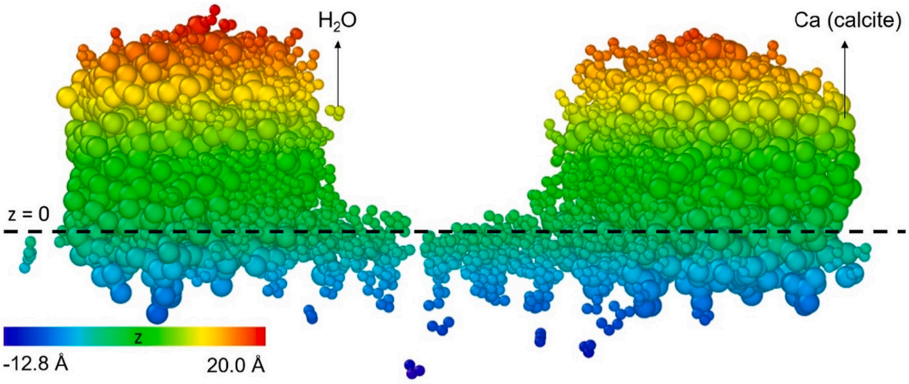

Fig. 7. Penetration of H_2O and Ca_2CO_3 atoms into SiO_2 (w_w = 66%). Note: where SiO_2 atoms have been removed for better visualization, and H_2O atoms have been depicted by smaller particles to avoid confusion with Ca atoms. The z = 0 line represents the elevation of the substrate atom having the highest *z* coordinate.

in other studies [55,56].

Results of MD simulations demonstrated that the interaction between calcite and the substrates could significantly be affected by the mineralogy and surface chemistry of soil grains, suggesting that the difference in the UCS of the EICP-treated sands can be due to the influence of coating minerals on the inter-particle bond strength. Calcite was found to interact with the substrates through two mechanisms: i) adhering to the substrate via nonbonded interactions, which were weaker in the presence of iron minerals on the surface, and ii) diffusing into the crystal structure of the substrates. As shown in Fig. 6 and Fig. 7, more calcite molecules diffused into silica than the other substrates both in dry and wet conditions. This observation suggests a stronger interlocking between calcite and silica at the molecular scale and consequently a higher interfacial bond strength and explains the higher bond strength in the EICP-treated Ottawa 1 sand that had a less amount of iron minerals on the surface.

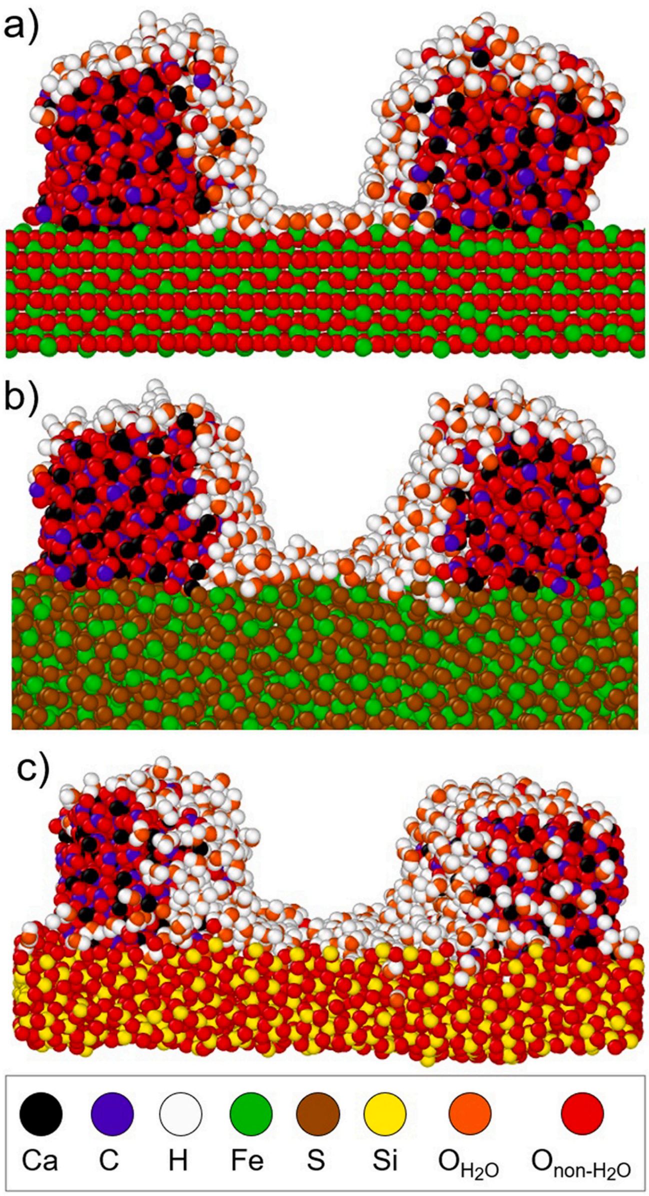

Fig. 8. Relaxed configuration of precipitates ($w_w = 66\%$) on a) Fe_2O_3, b) FeS_2, and c) SiO_2. Atoms are shown as color-coded circles.

4. Conclusion

Two types of Ottawa sand sharing identical geotechnical properties but differing in surface chemistry were treated via enzyme-induced carbonate precipitation (EICP) and tested for unconfined compressive strength (UCS). The considerable difference observed between the UCS of the two samples was hypothesized to be attributed to surface chemistry. This hypothesis was tested using molecular dynamics simulations of the interactions between calcite as the representative of minerals precipitated through EICP and substrates representing the surface of soil grains. The substrates included quartz (SiO_2), hematite (Fe_2O_3), and marcasite (FeS_2). Both dry (calcite–substrate) and hydrated (calcite–water–substrate) models were simulated. Simulation of the dry models revealed that calcite had the strongest affinity for SiO_2, suggesting that clean sand provides the most favorable host for precipitation. It was also observed that the presence of water led to reduced precipitate–grain adhesion. This study is the first to simulate biocementation at the nanoscale and demonstrates the capability of atomistic simulations to illuminate the mechanisms governing biocementation.

Supplementary data to this article can be found online at https://doi.org/10.1016/j.bpc.2022.106793.

Declaration of Competing Interest

The authors do not have any competing interests to declare.

Acknowledgments

This material is based upon work supported by the U.S. National Science Foundation under Grants CMMI 2046332 and EEC 1449501. Any opinions, findings, and conclusions or recommendations expressed in this material are those of the authors and do not necessarily reflect the views of the National Science Foundation. Some of the computing for this project was performed at the OU Supercomputing Center for Education & Research (OSCER) at the University of Oklahoma (OU). The authors also acknowledge Research Computing at Arizona State University for providing HPC resources that have contributed to the research results reported within this paper.

References

[1] L.A. van Paassen, R. Ghose, T.J. van der Linden, W.R. van der Star, M.C. van Loosdrecht, Quantifying biomediated ground improvement by ureolysis: large-scale biogrout experiment, J. Geotech. Geoenviron. 136 (2010) 1721–1728.

[2] A.B. Cunningham, R. Gerlach, L. Spangler, A.C. Mitchell, S. Parks, A. Phillips, Reducing the risk of well bore leakage of CO2 using engineered biomineralization barriers, Energy Procedia 4 (2011) 5178–5185.

[3] J.M. Minto, E. MacLachlan, G. El Mountassir, R.J. Lunn, Rock fracture grouting with microbially induced carbonate precipitation, Water Resour. Res. 52 (2016) 8827–8844.

[4] N. Hamdan, E. Kavazanjian, Enzyme-induced carbonate mineral precipitation for fugitive dust control, Géotechnique. (2016), https://doi.org/10.1680/jgeot.15.P.168.

[5] S. Gowthaman, S. Mitsuyama, K. Nakashima, M. Komatsu, S. Kawasaki, Biogeotechnical approach for slope soil stabilization using locally isolated bacteria and inexpensive low-grade chemicals: a feasibility study on Hokkaido expressway soil, Japan, Soils Found. 59 (2019) 484–499.

[6] H. Kou, C. Wu, P. Ni, B.-A. Jang, Assessment of erosion resistance of biocemented sandy slope subjected to wave actions, Appl. Ocean Res. 105 (2020), 102401.

[7] J. Lian, H. Xu, X. He, Y. Yan, D. Fu, S. Yan, H. Qi, Biogrouting of hydraulic fill fine sands for reclamation projects, Mar. Georesour. Geotechnol. 37 (2019) 212–222.

[8] P. Xiao, H. Liu, Y. Xiao, A.W. Stuedlein, T.M. Evans, Liquefaction resistance of biocemented calcareous sand, Soil Dyn. Earthq. Eng. 107 (2018) 9–19.

[9] A. Zamani, P. Xiao, T. Baumer, T.J. Carey, B. Sawyer, J.T. DeJong, R.W. Boulanger, Mitigation of liquefaction triggering and foundation settlement by MICP treatment, J. Geotech. Geoenviron. 147 (2021) 04021099, https://doi.org/10.1061/(ASCE)GT.1943-5606.0002596.

[10] K.K. Martin, H. Khodadadi Tirkolaei, E. Kavazanjian, Mid-scale biocemented soil columns via enzyme-induced carbonate precipitation (EICP), Soils Found. (2021), https://doi.org/10.1016/j.sandf.2021.09.001.

[11] T. Hamed Khodadadi, E. Kavazanjian, L. van Paassen, J. DeJong, Bio-grout materials: a review, Grouting 2017 (2017) 1–12.

[12] J.T. DeJong, M.B. Fritzges, K. Nüsslein, Microbially induced cementation to control sand response to undrained shear, J. Geotech. Geoenviron. 132 (2006) 1381–1392, https://doi.org/10.1061/(ASCE)1090-0241(2006)132:11(1381).

[13] V.S. Whiffin, L.A. van Paassen, M.P. Harkes, Microbial carbonate precipitation as a soil improvement technique, Geomicrobiol J. 24 (2007) 417–423, https://doi.org/10.1080/01490450701436505.

[14] H. Yasuhara, D. Neupane, K. Hayashi, M. Okamura, Experiments and predictions of physical properties of sand cemented by enzymatically-induced carbonate precipitation, Soils Found. 52 (2012) 539–549, https://doi.org/10.1016/j.sandf.2012.05.011.

[15] E. Kavazanjian, N. Hamdan, Enzyme Induced Carbonate Precipitation (EICP) Columns for Ground Improvement, 2015, pp. 2252–2261, https://doi.org/10.1061/9780784479087.209.

[16] A. Almajed, H. Khodadadi Tirkolaei, E. Kavazanjian, Baseline investigation on enzyme-induced calcium carbonate precipitation, J. Geotech. Geoenviron. 144 (2018) 04018081, https://doi.org/10.1061/(ASCE)GT.1943-5606.0001973.

[17] A. Almajed, H.K. Tirkolaei, E. Kavazanjian, N. Hamdan, Enzyme induced biocementated sand with high strength at low carbonate content, Sci. Rep. 9 (2019) 1135, https://doi.org/10.1038/s41598-018-38361-1.

[18] D.C. Rapaport, The Art of Molecular Dynamics Simulation, Cambridge University Press, Cambridge, UK, 2004.

[19] C. Zhang, Z. Liu, P. Deng, Contact angle of soil minerals: a molecular dynamics study, Comput. Geotech. 75 (2016) 48–56.

[20] C. Zhang, Z. Liu, P. Deng, Using molecular dynamics to unravel phase composition behavior of nano-size pores in frozen soils: does Young–Laplace equation apply in low temperature range? Can. Geotech. J. 55 (2018) 1144–1153.

[21] X. Tang, S. Xiao, Q. Lei, L. Yuan, B. Peng, L. He, J. Luo, Y. Pei, Molecular dynamics simulation of surfactant flooding driven oil-detachment in nano-silica channels, J. Phys. Chem. B 123 (2018) 277–288.

[22] N. Lu, C. Zhang, Soil sorptive potential: concept, theory, and verification, J. Geotech. Geoenviron. 145 (2019) 04019006.

[23] C. Zhang, X. Liu, X. Lu, E.J. Meijer, R. Wang, Understanding the heterogeneous nucleation of heavy metal phyllosilicates on clay edges with first-principles molecular dynamics, Environ. Sci. Technol. 53 (2019) 13704–13712.

[24] L. Liu, C. Zhang, W. Jiang, X. Li, Y. Dai, H. Jia, Understanding the sorption behaviors of heavy metal ions in the interlayer and nanopore of montmorillonite: a molecular dynamics study, J. Hazard. Mater. 416 (2021), 125976.

[25] H. Sun, W. Yang, R. Chen, X. Kang, Microfabric characteristics of kaolinite flocculates and aggregates—insights from large-scale molecular dynamics simulations, Appl. Clay Sci. 206 (2021), 106073.

[26] H. Ghasemi, H. Yazdani, A. Rajib, E.H. Fini, Toward carbon-negative and emission-curbing roads to drive environmental health, ACS Sustain. Chem. Eng. 10 (2022) 1857–1862, https://doi.org/10.1021/acssuschemeng.1c07356.

[27] V. Krishnan, H. Khodadadi Tirkolaei, K. Martin, N. Hamdan, L.A. Van Paassen, E. Kavazanjian Jr., Variability in the unconfined compressive strength of EICP-treated "standard" sand, J. Geotech. Geoenviron. 147 (2021) 06021001.

[28] H. Khodadadi Tirkolaei, N. Javadi, V. Krishnan, N. Hamdan, E. Kavazanjian, Crude urease extract for biocementation, J. Mater. Civ. Eng. 32 (2020) 04020374, https://doi.org/10.1061/(ASCE)MT.1943-5533.0003466.

[29] K. Kavitha, S. Sivakumar, B. Ramesh, 1,2,4 triazolo[1,5-a] pyrimidin-7-ones as novel SARS-CoV-2 Main protease inhibitors: in silico screening and molecular dynamics simulation of potential COVID-19 drug candidates, Biophys. Chem. 267 (2020), 106478, https://doi.org/10.1016/j.bpc.2020.106478.

[30] H. Ghasemi, H. Yazdani, E.H. Fini, Y. Mansourpanah, Interactions of SARS-CoV-2 with inanimate surfaces in built and transportation environments, Sustain. Cities Soc. 72 (2021), 103031, https://doi.org/10.1016/j.scs.2021.103031.

[31] L. González-Paz, M.L. Hurtado-León, C. Lossada, F.V. Fernández-Materán, J. Vera-Villalobos, M. Loroño, J.L. Paz, L. Jeffreys, Y.J. Alvarado, Comparative study of the interaction of ivermectin with proteins of interest associated with SARS-CoV-2: a computational and biophysical approach, Biophys. Chem. 278 (2021), 106677, https://doi.org/10.1016/j.bpc.2021.106677.

[32] K. Martin, H.K. Tirkolaei, E. Kavazanjian, Enhancing the strength of granular material with a modified enzyme-induced carbonate precipitation (EICP) treatment solution, Constr. Build. Mater. 271 (2021), 121529.

[33] X. Xu, H. Guo, M. Li, X. Deng, Bio-cementation improvement via CaCO3 cementation pattern and crystal polymorph: a review, Constr. Build. Mater. 297 (2021), 123478, https://doi.org/10.1016/j.conbuildmat.2021.123478.

[34] C.O. Sauer, Geography of the Upper Illinois Valley and History of Development, Illinois State Geological Survey, University of Illinois, 1916.

[35] C.L. Dake, The Problem of the St, Columbia University, Peter Sandstone, 1921.

[36] J.E. Lamar, Geology and economic resources of the St. Peter Sandstone of Illinois, Bulletin No. 053 (1928).

[37] S.A. Tyler, Heavy minerals of the Saint Peter sandstone in Wisconsin, J. Sediment. Res. 6 (1936) 55–84.

[38] R.T. Downs, M. Hall-Wallace, The American Mineralogist crystal structure database, Am. Mineral. 88 (2003) 247–250.

[39] S. Plimpton, Fast parallel algorithms for short-range molecular dynamics, J. Comput. Phys. 117 (1995) 1–19, https://doi.org/10.1006/jcph.1995.1039.

[40] A. Stukowski, Visualization and analysis of atomistic simulation data with OVITO–the open visualization tool, Model. Simul. Mater. Sci. Eng. 18 (2009), 015012, https://doi.org/10.1088/0965-0393/18/1/015012.

[41] J.V.L. Beckers, C.P. Lowe, S.W. De Leeuw, An iterative PPPM method for simulating coulombic systems on distributed memory parallel computers, Mol. Simul. 20 (1998) 369–383, https://doi.org/10.1080/08927029808022044.

[42] T.T.B. Le, A. Striolo, D.R. Cole, Supercritical CO2 effects on calcite wettability: a molecular perspective, J. Phys. Chem. C 124 (2020) 18532–18543, https://doi.org/10.1021/acs.jpcc.0c03210.

[43] D.J. Price, C.L. Brooks, A modified TIP3P water potential for simulation with Ewald summation, J. Chem. Phys. 121 (2004) 10096–10103, https://doi.org/10.1063/1.1808117.

[44] C.A. Latorre, J.P. Ewen, C. Gattinoni, D. Dini, Simulating surfactant–iron oxide interfaces: from density functional theory to molecular dynamics, J. Phys. Chem. B 123 (2019) 6870–6881, https://doi.org/10.1021/acs.jpcb.9b02925.

[45] M.R. Philpott, I.Y. Goliney, T.T. Lin, Molecular dynamics simulation of water in a contact with an iron pyrite FeS2 surface, J. Chem. Phys. 120 (2004) 1943–1950, https://doi.org/10.1063/1.1635362.

[46] A. Anagnostopoulos, A. Alexiadis, Y. Ding, Simplified force field for molecular dynamics simulations of amorphous SiO2 for solar applications, Int. J. Therm. Sci. 160 (2021), 106647, https://doi.org/10.1016/j.ijthermalsci.2020.106647.

[47] S. Nosé, A unified formulation of the constant temperature molecular dynamics methods, J. Chem. Phys. 81 (1984) 511–519, https://doi.org/10.1063/1.447334.

[48] W.G. Hoover, Canonical dynamics: equilibrium phase-space distributions, Phys. Rev. A 31 (1985) 1695–1697, https://doi.org/10.1103/PhysRevA.31.1695.

[49] R.A. Buckingham, J.E. Lennard-Jones, The classical equation of state of gaseous helium, neon and argon, Proceedings of the Royal Society of London. Series A. Mathematical and Physical Sciences. 168 (1938) 264–283, https://doi.org/10.1098/rspa.1938.0173.

[50] S. Munetoh, T. Motooka, K. Moriguchi, A. Shintani, Interatomic potential for Si–O systems using Tersoff parameterization, Comput. Mater. Sci. 39 (2007) 334–339, https://doi.org/10.1016/j.commatsci.2006.06.010.

[51] W.L. Jorgensen, J. Chandrasekhar, J.D. Madura, R.W. Impey, M.L. Klein, Comparison of simple potential functions for simulating liquid water, J. Chem. Phys. 79 (1983) 926–935, https://doi.org/10.1063/1.445869.

[52] K. Indulekha, R.E. Roy, A.G. Vishnu, R.S. Rajeev, K.N. Ninan, C. Gouri, Silicone copolymers bearing reactive vinyl and hydride functionalities: synthesis, characterisation and particulate composite thereof for specialty applications, Mater. Chem. Phys. 206 (2018) 213–223, https://doi.org/10.1016/j.matchemphys.2017.12.016.

[53] D. Lu, W. Cheng, T. Zhang, X. Lu, Q. Liu, J. Jiang, J. Ma, Hydrophilic Fe2O3 dynamic membrane mitigating fouling of support ceramic membrane in ultrafiltration of oil/water emulsion, Sep. Purif. Technol. 165 (2016) 1–9, https://doi.org/10.1016/j.seppur.2016.03.034.

[54] F.-X. Liang, L. Liang, X.-Y. Zhao, X.-W. Tong, J.-G. Hu, Y. Lin, L.-B. Luo, Y.-C. Wu, Mesoporous anodic α-Fe2O3 interferometer for organic vapor sensing application, RSC Adv. 8 (2018) 31121–31128, https://doi.org/10.1039/C8RA06261G.

[55] J. Zhao, G. Yao, S.B. Ramisetti, R.B. Hammond, D. Wen, Molecular dynamics investigation of substrate wettability alteration and oil transport in a calcite nanopore, Fuel. 239 (2019) 1149–1161.

[56] N.A. Wojas, I. Dobryden, V. Wallqvist, A. Swerin, M. Jarn, J. Schoelkopf, P. A. Gane, P.M. Claesson, Nanoscale Wear and mechanical properties of calcite: effects of stearic acid modification and water vapor, Langmuir. 37 (2021) 9826–9837.